

Perovskite-Type CuNbO_3 Exhibiting Unusual Noncollinear Ferrielectric to Collinear Ferroelectric Dipole Order Transition

Masayuki Fukuda,[†] Ikuya Yamada,[‡] Hidenobu Murata,[‡] Hajime Hojo,[§] Olivier J. Hernandez,^{||} Clemens Ritter,⁺ Katsuhisa Tanaka,[†] and Koji Fujita^{*†}

[†]Department of Material Chemistry, Graduate School of Engineering, Kyoto University, Katsura, Nishikyo-ku, Kyoto 615-8510, Japan

[‡]Department of Materials Science, Graduate School of Engineering, Osaka Prefecture University, 1-1 Gakuen-cho, Nakaku, Sakai, Osaka 599-8531, Japan

[§]Department of Advanced Materials Science and Engineering, Faculty of Engineering Sciences, Kyushu University, 6-1 Kasuga-koen, Kasuga, Fukuoka 816-8580, Japan

^{||}Univ Rennes, CNRS, ISCR (Institut des Sciences Chimiques de Rennes) - UMR 6226, F-35000 Rennes, France

⁺Institut Laue-Langevin, 71 avenue des Martyrs, Grenoble 38000, France

ABSTRACT: We report a perovskite oxide with a new type of polar structure, CuNbO_3 , thanks to the use of high-pressure and high-temperature synthesis. The perovskite-type CuNbO_3 was previously obtained under high-pressure and high-temperature conditions, but its crystal structure has not been solved yet. Our structural analysis reveals that CuNbO_3 perovskite crystallizes in a polar monoclinic space group (Pc) with a $\sqrt{2}a_{\text{pc}} \times \sqrt{2}a_{\text{pc}} \times 2a_{\text{pc}}$ unit cell (a_{pc} being the pseudo-cubic lattice parameter), which is one maximal non-isomorphic subgroup of the polar rhombohedral space group $R3c$. This compound exhibits a remarkable “noncollinear ferrielectric” structure, due to parallel displacements of Cu^+ and antiparallel displacements of Nb^{5+} along different axes, representing a new type of polar phase in the perovskite structure. We also observe that the noncollinear ferrielectric Pc structure transforms around 470 K into the collinear ferroelectric $R3c$ structure that features parallel displacements of Cu^+ and Nb^{5+} in the same direction. The present work extends the accessible composition range of the perovskite niobate series and demonstrates the role of A -O covalency in determining their crystal structure.

1. INTRODUCTION

Perovskite niobates, $\text{ANb}^{5+}\text{O}_3$ ($A = \text{Li}, \text{Na}, \text{K}, \text{and Ag}$), constitute an important class of oxide materials, exhibiting a wide range of properties including piezoelectricity, ferroelectricity, antiferroelectricity, and electro-optical and nonlinear optical effects.^{1–4} Recently, they also have attracted much attention due to their excellent photocatalytic and photovoltaic properties.^{5–7}

The lattice instabilities and structural distortions of perovskite oxides are often discussed in terms of the tolerance factor, $t = R_{A-O}/\sqrt{2} (R_{B-O})$, where R_{A-O} and R_{B-O} are the ideal A -O and B -O bond lengths for a particular ABO_3 material, respectively, calculated using the bond valence model⁸. For example, KNbO_3 is ferroelectric with $t > 1$ ($t = 1.06$), displaying so-called B -site driven ferroelectricity.^{9–11} The B -site cation (i.e., Nb^{5+}) is nominally too small for its octahedral site and can off center. In the room-temperature phase of KNbO_3 , second-order Jahn-Teller distortions^{12–14} for $\text{Nb}^{5+}(4d^0)$ ions yield their off-center displacements along the pseudo-cubic $\langle 110 \rangle_{\text{pc}}$ axis, leading to an orthorhombic ferroelectric structure (space group $\text{Amm}2$). Conversely, LiNbO_3 is ferroelectric with $t < 1$ ($t = 0.85$), exhibiting A -site driven ferroelectricity.^{15, 16} It can be described by a grossly

distorted perovskite-type structure. Generally, perovskites with $t < 1$ are not ferroelectric at all, and instead find favorable bond lengths through tilts of BO_6 octahedra about various axes, which preserve the inversion symmetry. The notable exceptions, including LiNbO_3 , are perovskites with very small t values, where a combination of the out-of-phase tilts of BO_6 octahedra around the $[111]_{\text{pc}}$ axis ($a^-a^-a^-$ tilt system in Glazer notation¹⁷) and polar displacements of A -site cations along the same axis yield a rhombohedral ferroelectric structure (space group $R3c$).

Since the t values of NaNbO_3 ($t = 0.97$) and AgNbO_3 ($t = 0.97$) are slightly less than 1, the coexistence of off-center Nb displacements and NbO_6 octahedral tilts provides complex crystal structures and phase diagrams.^{19–26} The room-temperature phase of NaNbO_3 is characterized by a sequence of two octahedral tilts system ($a^-a^-c^-/a^-a^-c^-$), and adopts an orthorhombic antiferroelectric structure (space group $Pbcm$), where the displacements of Nb^{5+} ions as well as of Na^+ ions are ordered in an antiferroelectric way and thereby the respective dipole moments are cancelled within the unit cell.^{18, 22} Despite the similar ionic radii (twelve-coordinated) of Ag^+ (1.37 Å) and Na^+ (1.39 Å), AgNbO_3 crystallizes in a different structure from NaNbO_3 . Recent

studies have revealed that AgNbO_3 is ferroelectric at room temperature, forming an orthorhombic ferroelectric structure (space group $Pmc2_1$).²⁶ The $Pmc2_1$ AgNbO_3 exhibits the same octahedral tilts system as the $Pbcm$ NaNbO_3 , but their cation displacements are ordered in a different way. In the case of AgNbO_3 , both displacements of Ag^+ and Nb^{5+} ions are ordered in a ferroelectric way, and thus the respective dipole moments are not completely cancelled within the unit cell. The uncompensated ionic displacements lead to a net polarization and weak ferroelectricity.^{25, 26} Here, it should be noted that the ordered dipole moments from the displacements of Ag^+ and Nb^{5+} ions are collinear to the $\langle 100 \rangle_{\text{pc}}$ axis. Namely, AgNbO_3 adopts a collinear ferroelectric structure. Yashima and Matsuyama pointed out that the formation of ferroelectric structure is ascribed to covalency of Ag–O bonds as well as of Nb–O bonds; the covalent character arises from the Ag 4d–O 2p and Nb 4d–O 2p orbital overlaps.²⁷ The Ag–O and Nb–O covalencies are also responsible for visible photocatalytic properties of AgNbO_3 .

Given the versatility and functionality of perovskite niobates, it is interesting to extend their compositional space to other systems. In this study, Cu^+ -based perovskite niobate, CuNbO_3 , is targeted because of the expectation that as in the case of AgNbO_3 , the covalent A–O and B–O bonding due to Cu 3d–O 2p and Nb 4d–O 2p orbital overlaps would result in an unusual electric dipole order. However, although ANbO_3 (A = Li, Na, K, and Ag) can be synthesized under ambient conditions, CuNbO_3 crystallizes in a nonperovskite structure in such conditions; the ambient-pressure phase of CuNbO_3 (AP- CuNbO_3) adopts a RbTaO_3 -type structure with a nonpolar monoclinic $C2/m$ symmetry.^{28, 29} AP- CuNbO_3 is characterized by a corner- and edge-sharing NbO_6 lamellar structure, in contrast to the perovskite structure with corner-sharing NbO_6 octahedra. Utilizing an ion exchange in AP- CuNbO_3 , a new form of LiNbO_3 with a lamellar structure was synthesized for the electrochemical applications.³⁰ The perovskite instability in CuNbO_3 is partly ascribed to the small Cu^+ ions on the A-sites, leading to a small t value ($t = 0.89$). We show here that the powerful high-pressure synthesis allows us to isolate a polar CuNbO_3 perovskite. The application of high pressure stabilizes phases that are inaccessible metastable products under ambient pressures. In particular, new perovskites and related oxides have emerged through exploration of the high-pressure and high-temperature phases of ABO_3 ternary systems.^{31, 32} In 1970, Sleight *et al.* reported the synthesis of a monoclinic perovskite-type CuNbO_3 at 6.5 GPa and 1273–1473 K, but no space group was unambiguously identified.³³ Clearly, the crystal structure of high-pressure-synthesized CuNbO_3 (HP- CuNbO_3) has remained elusive so far.

Herein, we present a comprehensive structural characterization of the metastable perovskite phase of HP-

CuNbO_3 using X-ray, neutron, and electron diffraction as well as optical second harmonic generation, combined with first-principles lattice dynamics calculations. The results show that HP- CuNbO_3 crystallizes in a monoclinic perovskite-type structure (space group Pc), featuring an unusual electric dipole order that represents a new type of polar phase in the perovskite structure. The perovskite-type Pc phase is a weakly polar material due to a “noncollinear ferroelectric” dipole order, i.e., a combination of parallel displacements of Cu^+ ions along $[111]_{\text{pc}}$ with respect to the closed-packed oxygen planes and antiparallel displacements of Nb^{5+} ions along $\langle 100 \rangle_{\text{pc}}$ with respect to the octahedral centroids. We also observe that, upon heating to 470 K in ambient pressure, the weakly polar Pc phase transforms into the strongly polar $R3c$ phase with parallel displacements of Cu^+ and Nb^{5+} ions. Our results highlight that the bonding nature of A-site cations, as well as their ionic size, has great impact on electric dipole order in small-tolerance-factor perovskites.

2. EXPERIMENTAL AND COMPUTATIONAL DETAILS

Polycrystalline samples of CuNbO_3 were prepared by the solid-state reaction at high pressure and high temperature. Stoichiometric amounts of the starting materials, Cu_2O (99.9%, Rare Metallic) and Nb_2O_5 (99.99%, Sigma-Aldrich) were ground and mixed carefully. The mixed powder was placed into a Pt capsule and put into a high-pressure cell. The solid-state reaction was performed at 12 GPa and 1273 K for 30 min with a Walker-type high-pressure apparatus, followed by a rapid temperature quench and then a gradual pressure release.

Electron diffraction (ED) patterns were taken from single-crystal domains at room temperature using a JEM-ARM200F (JEOL) transmission electron microscope. Synchrotron X-ray diffraction (SXRD) data were recorded at room temperature ($\lambda = 0.75003 \text{ \AA}$) and in the temperature range of 300 to 680 K ($\lambda = 0.77565 \text{ \AA}$) on the BL02B2 beamline at SPring-8. The powder sample was loaded into a Lindemann glass capillary with an inner diameter of 0.1 mm, continuously rotated during the measurement to reduce the effect of preferential orientation. Neutron powder diffraction (NPD) data were collected at room temperature on the D2B instrument at the Institut Laue-Langevin, Grenoble ($\lambda = 1.594 \text{ \AA}$). A 475.7-mg sample was encased in a vanadium can. The crystal structure was refined using the Rietveld analysis programs Fullprof³⁴ and JANA2006.³⁵ In the former case, a Thompson-Cox-Hastings pseudo-Voigt profile function was used, as well the Berar & Baldinozzi model for asymmetry correction. Anisotropic broadening was taken into account through spherical harmonics coefficient (size effect) or generalized S_{HKL} strain parameters. The width of few isolated reflections was additionally selectively relaxed. An absorption correction

was applied for the SXRD refinement. DICVOL06³⁶ was used to index the diffraction pattern. The structure solution was carried out through the direct method with EXPO2013.³⁷ The crystal structures were drawn using the program VESTA³⁸ based on the structural refinement results. The cation ratio within the sample was determined with inductively coupled plasma optical emission spectroscopy (ICP-OES) on a SPECTROBLUE (SPECTRO).

To investigate the presence of noncentrosymmetry, a second-harmonic generation (SHG) response was measured at room temperature using a pulsed Nd:YAG laser (λ , 1064 nm; pulse duration, 25 ps; repetition frequency, 10 Hz) as the light source. The SHG light from the sample was detected with a photomultiplier tube through a 532-nm narrow band-pass filter. X-ray absorption near edge structure (XANES) spectroscopy at Cu and Nb *K*-edges were collected by the transparent method on the BL14B2 beamline at SPring-8. The magnetic susceptibility data were recorded using a SQUID magnetometer MPMS-XL (Quantum Design) between 5 and 300 K under an applied field of 100 Oe.

Electronic and crystal structure of CuNbO₃ and related compounds were calculated within the framework of density functional theory using the projector augmented-wave (PAW) method³⁹ implemented in the Vienna Ab-initio Simulation Package (VASP) code.^{40–42} The cut-off energy of plane waves set to 600 eV. The *k*-points sampling was performed by Γ -centered Monkhorst-Pack⁴³ 4×4×3, 4×4×4, and 6×6×6 meshes for *Pc* perovskite-type and *R3c* LiNbO₃-type CuNbO₃ and Cu₂O, respectively. Exchange-correlational functional were evaluated with the PBEsol functional.⁴⁴ The effect of Hubbard *U* was considered using Dudarev's approach.⁴⁵ The effective on-site Coulomb term, U_{eff} , was set at 3 eV. The initial electronic configurations for PAW potentials were 3s² 3p⁶ 3d¹⁰ 4p¹, 1s² 2s¹, 4s² 4p⁶ 5s² 4d³, and 2s² 2p⁶ for Cu, Li, Nb, and O, respectively. The crystal structures were fully optimized until residual forces and stresses were less than 1.0×10^{−4} eV Å^{−3} and 1.0×10^{−3} eV Å^{−3}, respectively. Convergence tests were performed by comparing the results with more severe conditions, e.g., 800 eV and two times denser *k*-meshes. We confirmed that total energies were converged within 3 meV atoms^{−1}.

Lattice dynamics calculations were performed using Parlinski-Li-Kawazoe method implemented by phonopy code.^{46–50} We used 2×2×2 rhombohedral supercell for LiNbO₃-type CuNbO₃.

We also performed Cu-*K* XANES calculations with the full-potential linearized augmented plane wave plus local orbitals method and the PBEsol + *U* (U_{eff} = 3 eV) functional available in the WIEN2k code.^{51, 52} A core-hole was directly treated for final state calculations. The cut-off parameter of the plane wave, $R_{\text{MT}}K_{\text{MAX}}$, was set to 6.0 bohr Ry^{1/2}. Calculated spectra were broadened by Lorentz functions with a natural width of Cu-*K* shell.⁵³ To correct the

calculated transition energies, the calculated Cu-*K* XANES spectra in the present study were shifted by −29.0 eV, which corresponds to a transition-energy difference between the theoretical and experimental Cu-*K* XANES for the reference material, Cu₂O.

3. RESULTS

3.1. Crystal Structure: HP-CuNbO₃ was previously prepared at 6.5 GPa and 1273 – 1473 K and reported to adopt a monoclinic symmetry with $a = 3.836 \text{ \AA}$ ($\approx a_{\text{pc}}$), $b = 10.432 \text{ \AA}$ ($\approx 2\sqrt{2}a_{\text{pc}}$), $c = 5.546 \text{ \AA}$ ($\approx \sqrt{2}a_{\text{pc}}$), and $\beta = 94.66^\circ$.³³ In this study, we found that the higher-purity samples tend to be obtained by the use of the higher synthesis pressure (~12 GPa) (see **Figure S1** in Supporting Information).

First, we performed ED for the high-purity samples to deduce the crystal symmetry of HP-CuNbO₃. **Figure 1** shows the ED patterns at room temperature along the [001], [010], and [100] zone axes. In contrast to the previous report,³³ all reflections can be indexed with another monoclinic cell with $a \approx 5.5 \text{ \AA}$ ($\approx \sqrt{2}a_{\text{pc}}$), $b \approx 5.2 \text{ \AA}$ ($\approx \sqrt{2}a_{\text{pc}}$), $c \approx 7.7 \text{ \AA}$ ($\approx 2a_{\text{pc}}$), and $\beta \approx 95^\circ$. The observations of 120 reflection at [001] and 012 reflection at [100] (see red circles in **Figure 1**) are indicative of a primitive monoclinic unit cell. The absence of 00*l* reflections with *l* = odd (e.g., 001 reflection) in the [010] pattern reveals the presence of the *c*-glide symmetry. The finite intensity of the forbidden 001 reflection along [100] is due to multiple scattering effects. Given the 0*k*0 reflections with *k* = odd (e.g., 010 reflections) in the [001] and [100] zone axes, one will expect the absence of the 2₁ screw axis. However, when the multiple scattering effects are significant, the 010 reflections are observed even in the presence of the 2₁ screw axis. Namely, the presence or absence of the 2₁ screw axis cannot be determined by the ED analysis alone. We thus suggest possible space groups to be *Pc*, *P2*/*c*, or *P2*₁/*c*.

Next, we carried out SXRD and NPD experiments at 300 K to identify the crystal symmetry of HP-CuNbO₃. The main reflections seem at first sight to be indexed with a *R3c* (LiNbO₃-type) structure ($a \approx 5.2 \text{ \AA}$ and $c \approx 14.0 \text{ \AA}$ in a hexagonal setting), but the indexing of SXRD and NPD patterns with the successive dichotomy method³⁶ indicates a monoclinic cell $a \approx 5.5 \text{ \AA}$ ($\approx \sqrt{2}a_{\text{pc}}$), $b \approx 5.2 \text{ \AA}$ ($\approx \sqrt{2}a_{\text{pc}}$), $c \approx 7.7 \text{ \AA}$ ($\approx 2a_{\text{pc}}$) and $\beta \approx 95^\circ$, in good agreement with the ED analysis. Consistent with the symmetry lowering from the rhombohedral *R3c* structure, the peak splitting (e. g., 014_{*h*} and 110_{*h*}) and superstructure reflections (e. g., 012_{*m*} and 102_{*m*}) are detected in the SXRD pattern (**Figure 2a**), where the subscript *h* and *m* represent the hexagonal and monoclinic unit cells, respectively. The symmetry lowering from the *R3c* structure is also found from the peak splitting (e.g., 022_{*h*} and 024_{*h*}) in the NPD pattern (**Figure 2b**). The reflection conditions in the SXRD and NPD data, as well as in the ED data, leave *Pc*, *P2*/*c*, or *P2*₁/*c* as possible space groups. The *Pc* structure is noncentrosymmetric-polar,

while the $P2/c$ and $P2_1/c$ structures are centrosymmetric. To identify the space group of HP-CuNbO₃, we additionally measured the second-order nonlinear optical properties. Our experiments confirmed an SHG activity (**Figure S2** in Supporting Information), showing the noncentrosymmetric character. Therefore, the space group of HP-CuNbO₃ is found to be Pc .

The structural relationship between the Pc and $R3c$ phases is a maximal non-isomorphic group/subgroup with the following transformation matrix:

$$\begin{pmatrix} a_m \\ b_m \\ c_m \end{pmatrix} = \begin{pmatrix} -1/3 & -2/3 & 1/3 \\ -1 & 0 & 0 \\ -2/3 & -4/3 & -1/3 \end{pmatrix} \begin{pmatrix} a_h \\ b_h \\ c_h \end{pmatrix},$$

where a_m , b_m , and c_m are the lattice parameters of the monoclinic unit cell, and a_h , b_h , and c_h are the lattice parameters in the hexagonal setting of the rhombohedral $R3c$ unit cell. To the best of our knowledge, simple ABO_3 perovskites crystallizing in Pc with $a_m \approx \sqrt{2}a_{pc}$, $b_m \approx \sqrt{2}a_{pc}$, and $c_m \approx 2a_{pc}$ unit cell have not been discovered yet.

Rietveld refinements were performed against NPD and SXRD patterns of HP-CuNbO₃ at 300 K by assuming as an initial model a Pc unit cell with a $\sqrt{2}a_{pc} \times \sqrt{2}a_{pc} \times 2a_{pc}$ unit cell. The initial structural model was derived from the group-subgroup relationship with an $R3c$ (LiNbO₃-type) model using the program ISODISTORT of the ISOTROPY Software Suite,⁵⁴ and confirmed by structure solution against the SXRD data using direct methods. The Nb1 position is fixed to (0, 0, 0). **Figure 3a, b** displays the refinement results for SXRD and NPD data, respectively. For the SXRD data, the presence of heavy Nb and Cu atoms leads to a very low contrast for oxygen atoms. The B_{iso} of oxygen atoms were accordingly fixed to the B_{iso} value of Nb2. The stoichiometric composition models provide good overall fits to the observed patterns for both SXRD (weighted profile R factor $R_{wp} = 11.60\%$ and Bragg R factor $R_B = 6.62\%$) and NPD data ($R_{wp} = 10.34\%$ and $R_B = 3.66\%$). The cation site occupancies were refined to check deviations in the stoichiometry, but the refined occupancies remained within 1 or 2 % of the expected full site values. This result is in agreement with complementary ICP-OES analysis in which the cationic ratio is almost stoichiometric (Cu/Nb = 1.05) within standard uncertainties.

We also examined the possibility of cation mixing on the A-site. According to the previous structural analyses on LiNbO₃, the cation distribution was estimated to be $(Li_{1-5x}Nb_x\Box_{4x})NbO_3$, where \Box represents a vacancy.^{55, 56} In the course of our refinements against SXRD and NPD data, the introduction of a small amount of Nb (a few percent) at the Cu1 or Cu2 sites did not improve the fitting quality. The refined structural parameters from SXRD and NPD data are listed in **Table 1** and **Table 2**, respectively. The selected bond lengths and bond angles are tabulated in **Table S1**.

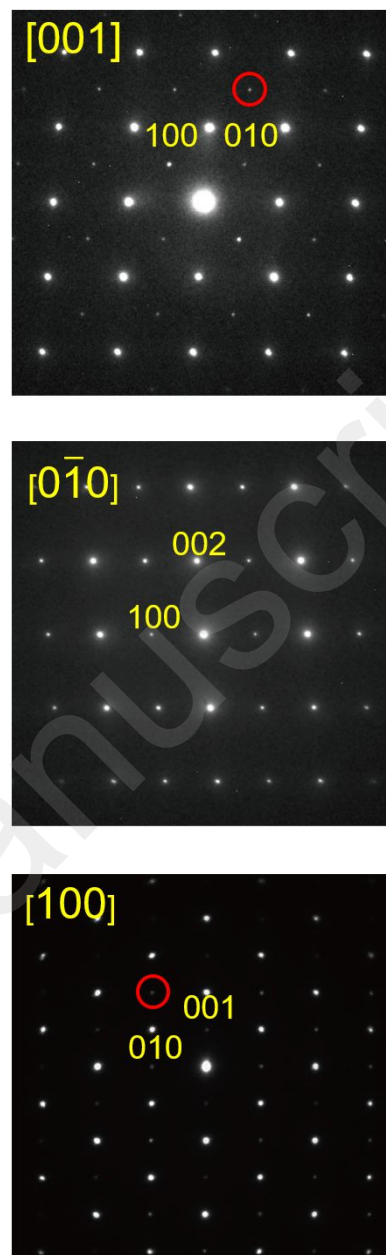


Figure 1. ED patterns of HP-CuNbO₃ at room temperature taken along [001], [010], and [100] zone axes. Representative indices are shown just above the corresponding reflection spots. The reflections marked in red are indicative of a primitive cell.

The calculated density of HP-CuNbO₃ [6.12 g cm⁻³ (SXRD) and 6.14 g cm⁻³ (NPD)] is significantly larger than that of AP-CuNbO₃ (5.02 g cm⁻³),²⁸ consistent with the expectation that the high-pressure synthesis provides a higher-density phase. Bond-valence-sum calculations⁸ using the NPD (SXRD)-refined bond lengths give +0.93(3) (+0.85(2)), +0.99(2) (+0.84(2)), +4.85(7) (+5.04(8)), and +4.84(8)

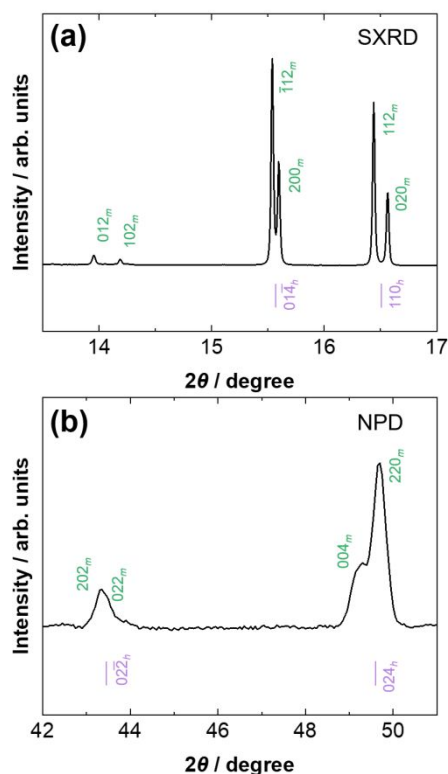


Figure 2. Enlarged portions of (a) SXRD ($\lambda = 0.75003 \text{ \AA}$) and (b) NPD ($\lambda = 1.594 \text{ \AA}$) patterns of HP-CuNbO₃ at 300 K. Some reflections in the observed patterns are split by a monoclinic distortion from the rhombohedral $R3c$ structure; the purple ticks correspond to the positions of the allowed Bragg reflections for the $R3c$ structure. The subscript h represents the rhombohedral unit cell in a hexagonal setting, and the subscript m indicates the monoclinic unit cell.

(+4.76(8)) for Cu1, Cu2, Nb1, and Nb2, respectively, confirming the Cu⁺Nb⁵⁺O₃ ionic model. This result conforms to those of XANES and temperature-dependent magnetic susceptibility experiments, which will be separately described below. **Figure 4** depicts the crystal structures of HP-CuNbO₃ refined against the NPD data at 300 K. The monoclinic distortion of HP-CuNbO₃ highlights the tilting distortion of NbO₆ octahedra and the off-center displacements of Nb⁵⁺ ions. The octahedral tilt system is $a^-a^-c^-$. Glazer¹⁷ has shown that this tilt system in an aristotype cubic $Pm\bar{3}m$ perovskite leads to a centrosymmetric monoclinic $C2/c$ structure. In HP-CuNbO₃ perovskite, the symmetry is lowered to the space group Pc by the two inequivalent off-center displacements of Nb⁵⁺ ions (see arrows in **Figure 4b**).

In ABO₃ perovskite oxides, the decrease in the A-site ionic radius, i.e., the reduction in the tolerance factor t , results in enhanced octahedral tilting, leading to the decrease of the

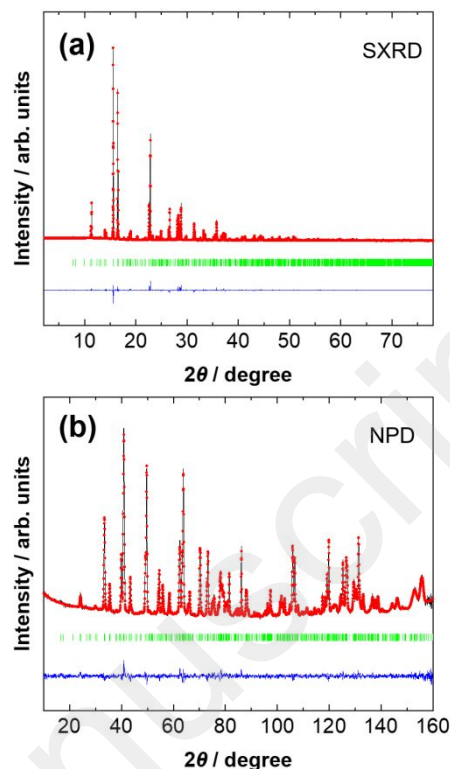


Figure 3. Rietveld refinements against (a) SXRD ($\lambda = 0.75003 \text{ \AA}$) and (b) NPD ($\lambda = 1.594 \text{ \AA}$) patterns of HP-CuNbO₃ at 300 K. These refinements were performed on the basis of the monoclinic Pc perovskite-type structure model with a $\sqrt{2}a_{pc} \times \sqrt{2}a_{pc} \times 2a_{pc}$ unit cell, showing the observed (red circles) and calculated (black solid lines) profiles. The blue solid lines represent the difference between the observed and calculated profiles. The green ticks correspond to the positions of the allowed Bragg reflections.

$B-O-B$ bond angle. As expected from the small t value ($t = 0.89$), the Pc phase of HP-CuNbO₃ possesses a notable magnitude of NbO₆ octahedral tilts, with the Nb-O-Nb angles deviating significantly from the ideal value of 180° by up to ~36° (see **Table S1**). The Nb-O-Nb bond angles of HP-CuNbO₃ (144–148°) are smaller than those of NaNbO₃ (157–162°),²² but are larger than that of LiNbO₃ (140°).¹⁵ Namely, the average Nb-O-Nb bond angle decreases in the order NaNbO₃ ($t = 0.97$) > CuNbO₃ ($t = 0.89$) > LiNbO₃ ($t = 0.85$), demonstrating the A-site-cation-size-dependent octahedral tilting. In Pc CuNbO₃, the coordination environments of the two independent Nb sites, Nb1 and Nb2, are strongly asymmetric, due to their off-center displacements along [001] ($=\langle 100 \rangle_{pc}$) within the octahedra (see **Figure 4b**). The NbO₆ octahedral distortion Δ of HP-CuNbO₃ was calculated from the NPD-refined bond lengths; $\Delta = 1/6 \sum_i [(d_i - \langle d \rangle) / \langle d \rangle]^2$, where d_i is the individual Nb-O bond length and $\langle d \rangle$ is the average Nb-O bond length

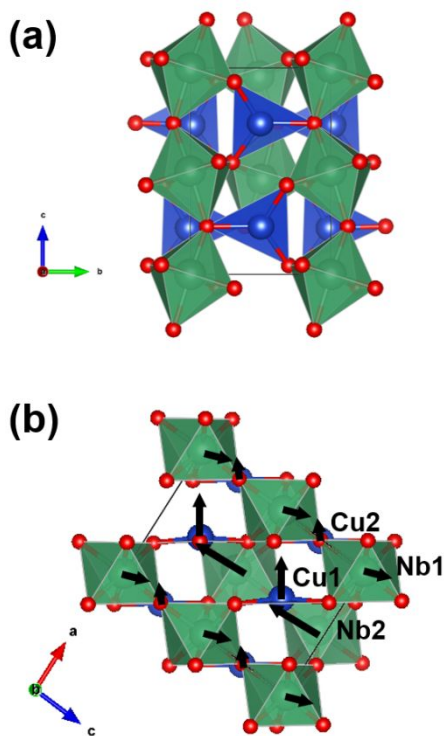


Figure 4. The refined crystal structures of HP-CuNbO₃ from the NPD data at 300 K. The structural views in (a) *bc* and (b) *ac* planes are shown. The arrows in (b) indicate the cation displacements from the closed-packed oxygen planes and those from the centroids of NbO₆ octahedra.

(see **Table S1**). We obtained $\Delta(\text{Nb1O}_6) = 1.5(2) \times 10^{-3}$ and $\Delta(\text{Nb2O}_6) = 2.9(1) \times 10^{-3}$. The magnitude of these octahedral distortions is comparable to that for other perovskite niobates ANbO_3 with second-order Jahn–Teller active $\text{Nb}^{5+}(4d^0)$ ions (e.g., $3.11(1) \times 10^{-3}$ for LiNbO_3 ¹⁵ and $4.0(3) \times 10^{-3}$ for KNbO_3).¹¹ The large octahedral distortions for HP-CuNbO₃ are thus ascribed to the second-order Jahn–Teller effects.

Asymmetric environments are also observed for the Cu coordination in *Pc* CuNbO₃: Cu atoms are displaced approximately along $[20\bar{3}]$ ($= [111]_{\text{pc}}$) with respect to the oxygen-triangle planes, occupying two independent Cu sites, Cu1 and Cu2 (see **Figure 4b**). Each of Cu1 and Cu2 atoms forms three shorter and nine longer bonds with the oxygen atoms (see also **Table S1**), although the *A*-site cations in aristotype perovskites are surrounded by 12 equidistant anions. The distances of the longer Cu–O bonds (2.64(3)–3.26(2) Å for Cu1 and 2.76(2)–3.20(2) Å for Cu2) are much larger than those of the shorter Cu–O bonds (2.01(3), 2.04(3), 2.08(1) Å for Cu1 and 2.00(1), 2.03(2), 2.03(2) Å for Cu2), and so the effective coordination number of Cu atoms is three. The coordination environments of Cu1O₃ and Cu2O₃ differ in terms of polyhedral distortions and average bond lengths. The displacement from the centers of oxygen triangles is about nine times larger for Cu1 than for Cu2 (see **Figure 4b** and **Figure 11**).

Table 1. Structural Parameters of HP-CuNbO₃ at 300 K Obtained from Refinements against the SXRD Data

atom	site	<i>g</i>	<i>x</i>	<i>y</i>	<i>z</i>	<i>U</i> _{iso} / Å ²
Cu1	2 <i>a</i>	1	0.5269(4)	0.9961(19)	0.2100(3)	0.0153(7)
Cu2	2 <i>a</i>	1	0.9986(4)	0.4953(17)	0.7206(3)	0.0082(6)
Nb1	2 <i>a</i>	1	0	0	0	0.0100(5)
Nb2	2 <i>a</i>	1	0.4910(3)	0.5074(6)	0.4513(2)	0.0020(3)
O1	2 <i>a</i>	1	0.183(3)	0.687(3)	0.428(2)	0.0020(3)
O2	2 <i>a</i>	1	0.691(3)	0.193(3)	0.928(2)	= <i>U</i> _{iso} (O1)
O3	2 <i>a</i>	1	0.289(3)	0.204(3)	0.537(2)	= <i>U</i> _{iso} (O1)
O4	2 <i>a</i>	1	0.791(3)	0.707(3)	0.028(2)	= <i>U</i> _{iso} (O1)
O5	2 <i>a</i>	1	0.962(2)	0.103(3)	0.227(1)	= <i>U</i> _{iso} (O1)
O6	2 <i>a</i>	1	0.475(2)	0.612(2)	0.716(1)	= <i>U</i> _{iso} (O1)

Space group: *Pc* (No. 7), *Z* = 4. CuNbO₃ (fw = 204.45 g mol^{−1}): $\lambda = 0.75003$ Å, 0.595 Å < *d* < 20.2 Å; lattice parameters: *a* = 5.54535(4) Å, *b* = 5.21029(3) Å, *c* = 7.67491(6) Å, $\beta = 94.6924(6)^\circ$, and *V* = 221.007(3) Å³, *R*_{wp} = 11.60 % and *R*_B = 6.62 %; $R_{\text{wp}} = [\sum w_i (y_{\text{io}} - y_{\text{ic}})^2 / \sum w_i y_{\text{io}}^2]^{1/2}$, where *y*_{io} and *y*_{ic} are the observed and calculated intensities, respectively, and *w_i* is the weighting factor. $R_{\text{B}} = \sum |I_{\text{o}}(h_K) - I_{\text{c}}(h_K)| / \sum |I_{\text{o}}(h_K)|$, where *I*_o(*h_K*) and *I*_c(*h_K*) are the observed and calculated integrated intensities for reflection *K*, respectively.

Table 2. Structural Parameters of HP-CuNbO₃ at 300 K Obtained from Refinements against the NPD Data

atom	site	<i>g</i>	<i>x</i>	<i>y</i>	<i>z</i>	<i>U</i> _{eq/iso} / Å ²
Cu1	2 <i>a</i>	1	0.514(4)	0.988(2)	0.226(2)	0.065(5)
Cu2	2 <i>a</i>	1	0.989(2)	0.498(2)	0.735(2)	0.011(1)
Nb1	2 <i>a</i>	1	0	0	0	0.094(13)
Nb2	2 <i>a</i>	1	0.4830(14)	0.5122(14)	0.4610(8)	0.015(2)
O1	2 <i>a</i>	1	0.184(2)	0.686(2)	0.433(2)	0.007(1)
O2	2 <i>a</i>	1	0.686(3)	0.185(2)	0.935(2)	0.014(2)
O3	2 <i>a</i>	1	0.290(3)	0.205(2)	0.546(2)	0.005(2)
O4	2 <i>a</i>	1	0.795(3)	0.701(2)	0.043(2)	0.002(2)
O5	2 <i>a</i>	1	0.993(3)	0.119(2)	0.233(2)	0.007(1)
O6	2 <i>a</i>	1	0.491(3)	0.613(2)	0.733(2)	0.008(2)

Space group: *Pc* (No. 7), *Z* = 4. CuNbO₃ (fw = 204.45 g mol⁻¹): λ = 1.594 Å, 0.809 Å < *d* < 6.11 Å; lattice parameters: *a* = 5.548088(10) Å, *b* = 5.208766(9) Å, *c* = 7.695716(15) Å, β = 94.67983(10)°, and *V* = 221.6547(7) Å³, *R*_{wp} = 10.34 % and *R*_B = 3.66 %. Cu1 was refined anisotropically.

Interestingly, we notice that the perovskite-type HP-CuNbO₃ has the same crystal symmetry and unit-cell metrics as the lowest-temperature monoclinic phase of WO₃, ε-WO₃.⁵⁷ Namely, both of them crystallize in *Pc* symmetry with *a_m* ≈ √2*a_{pc}*, *b_m* ≈ √2*a_{pc}*, and *c_m* ≈ 2*a_{pc}*. Note that the structure of WO₃ can be regarded as an ABO₃ perovskite-type structure with empty *A*-sites. In the *Pc* structure, the *B*1 and *B*2 atoms (*B* = Nb in HP-CuNbO₃ or W in ε-WO₃) undergo almost antiparallel off-center displacements along [001] (= <100>_{pc}) within the octahedra. For ε-WO₃, the antiparallel displacements of W1 and W2 atoms with different amplitudes produce “collinear ferrielectricity”. For HP-CuNbO₃, the antiparallel displacements of Nb1 and Nb2 with different magnitudes are accompanied by the parallel displacements of Cu1 and Cu2 atoms approximately along [203̄] (= [111]_{pc}). Consequently, a noncollinear ferrielectric structure appears in the *Pc* phase of HP-CuNbO₃. The spontaneous polarization calculated from the NPD-refined crystal structure using the formal charges of Cu⁺ and Nb⁵⁺ is 9.7 μC cm⁻².

It is worth underlining that ferrielectricity is observed in AgNbO₃, but it stems from collinear electric dipole order. On the other hand, HP-CuNbO₃ is a rare example of a ferrielectric material with noncollinear electric dipole order, representing a new type of polar phase in the perovskite structure.

3.2. Valence state: Figure 5a, b displays the experimental and calculated XANES spectra at the Cu *K*-edge, respectively. The experimental Cu absorption edge position of HP-CuNbO₃ is close to that of Cu₂O, but different from that of

CuO. The contrasting coordination environment between HP-CuNbO₃ (perovskite *A*-site) and Cu₂O (linear coordination), however, makes it difficult to estimate clearly the Cu valency in HP-CuNbO₃. So, we performed XANES calculations for HP-CuNbO₃ as well as for a reference compound, Cu₂O (Figure 5b). The experimental spectra for HP-CuNbO₃ and Cu₂O matches qualitatively the calculated spectra based on Cu⁺Nb⁵⁺O₃ and Cu⁺₂O models, respectively, revealing that the Cu cations are present as Cu⁺ in both compounds. On the other hand, the Nb valency in HP-CuNbO₃ can be easily estimated to be +5 from the similarity of its experimental spectrum to that of Nb₂O₅ (Figure 6). Thus, our XANES analyses unambiguously evidence that the valence states in CuNbO₃ are +1 for Cu and +5 for Nb.

Figure 7 gives the temperature dependence of magnetic susceptibility, χ(*T*), of HP-CuNbO₃ measured at 100 Oe after zero-field cooling. The fitting was carried out on the basis of the Curie–Weiss law described by the following equation:

$$\chi(T) = \chi_0 + \frac{N\mu_{\text{eff}}^2}{3k_B(T - \theta_w)},$$

where χ₀ is a temperature-independent term, *N* the Avogadro constant, μ_{eff} the effective magnetic moment, *k_B* the Boltzmann constant, and θ_w the Weiss temperature. The fitting results are χ₀ = −2.6(1) × 10^{−4} emu Oe^{−1} mol^{−1}, θ_w = −1.8(2) K, and μ_{eff} = 0.301(6) μ_B. The calculated effective magnetic moment is significantly smaller than that for Cu²⁺ (1.732 μ_B). The paramagnetic behavior is thus attributed to a small amount of magnetic impurities. In addition, χ(*T*) is negative above 50 K, with the absolute values being larger

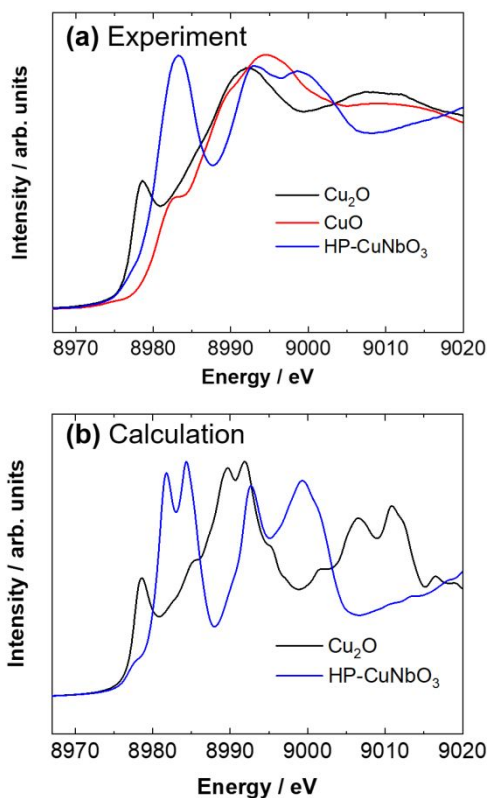


Figure 5. (a) The experimental Cu *K*-edge XANES spectrum of HP-CuNbO₃ (blue) in comparison with those of Cu₂O (black) and CuO (red). (b) The calculated Cu *K*-edge XANES spectra of HP-CuNbO₃ (blue) and Cu₂O (black).

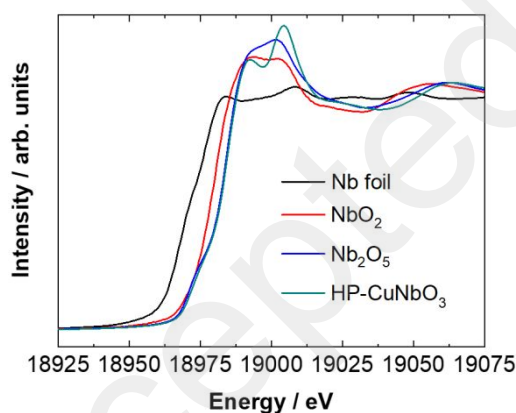


Figure 6. The experimental Nb *K*-edge XANES spectrum of HP-CuNbO₃ (green) in comparison with those of Nb foil (black), NbO₂ (red), and Nb₂O₅ (blue).

than those of the container used for the measurement. These facts mean that HP-CuNbO₃ is diamagnetic and has closed-shell cations, Cu⁺(d¹⁰) and Nb⁵⁺(d⁰).

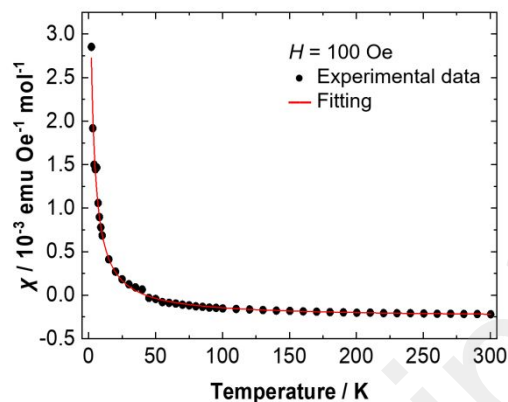


Figure 7. Temperature dependence of magnetic susceptibility, $\chi = M/H$, of HP-CuNbO₃ measured at $H = 100$ Oe after zero-field cooling. The dots represent the observed data, while the red solid line is the fitted curve according to the Curie–Weiss law.

3.3. Temperature-driven phase transition: Figure 8a,b shows temperature-variable SXRD patterns upon heating HP-CuNbO₃ above 300 K under ambient pressure. The heating rate was set to 20 K min⁻¹ and the waiting time at each temperature was 1 min. One can see that the peak splittings observed at 300 K, which arise from the monoclinic distortion, disappear at 470 K. This fact is indicative of the phase transition from a monoclinic *Pc* phase into a higher-symmetry rhombohedral phase. Considering the reflection conditions for the high-temperature phase in the hexagonal setting ($-h + k + l = 3n$ for *hkl*, $h + l = 3n$ and $l = 2n$ for *h \bar{h} l*, $l = 3n$ for *hhl*, and $l = 6n$ for *00l*), the possible space groups are either *R3c* (noncentrosymmetric polar) or *R $\bar{3}$ c* (centrosymmetric nonpolar).

To deduce the space group of the high-temperature rhombohedral polymorph, we examined the temperature variation of the lattice parameters between 470 and 510 K, and found that the a_h parameter increases with increasing temperature, while the temperature rise results in a decrease in the c_h parameter (see Figure S3 in Supporting Information). Similar behavior has been observed for *R3c* ferroelectric compounds, like LiNbO₃, LiTaO₃,⁵⁸ and LiOsO₃,⁵⁹ where the relaxation of the spontaneous ferroelectric strains along the *c* axis upon heating up to the Curie temperature (T_c) leads to a decrease of the c_h parameters and an increase of the a_h parameters; in the absence of spontaneous strains (i.e., in the high-temperature *R $\bar{3}$ c* phases at $T > T_c$), both a_h and c_h parameters increase with increasing temperature, as naturally expected. Judging from the thermal evolution of the c_h parameter for the high-temperature phase of HP-CuNbO₃ (i.e., decrease of the c_h parameter upon heating), its space group is determined as a polar *R3c*. In other words, HP-CuNbO₃ transforms upon heating at 470 K into *R3c* (LiNbO₃-type) CuNbO₃. The pseudo-cubic lattice volumes,

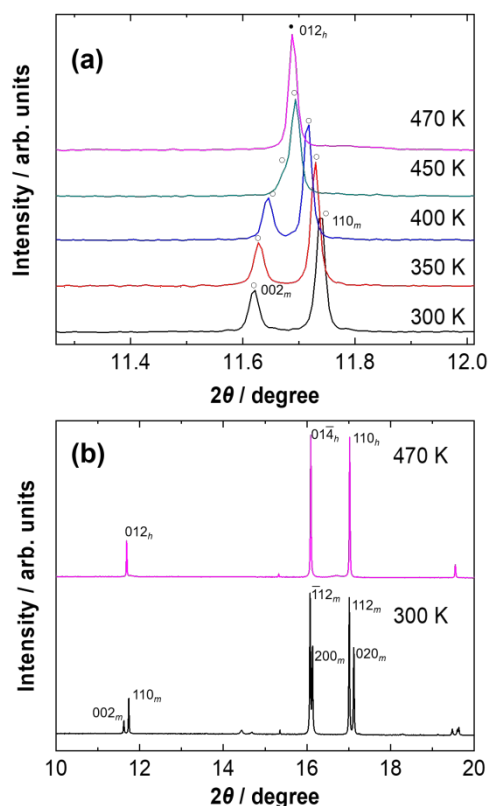


Figure 8. (a) Temperature evolution of SXRD patterns ($\lambda = 0.75565 \text{ \AA}$) of HP-CuNbO₃ in the temperature range of 300 to 470 K. (b) Comparison between SXRD patterns at 300 K (*Pc*) and at 470 K (*R3c*). The subscript *h* represents the rhombohedral unit cell in a hexagonal setting, and the subscript *m* indicates the monoclinic unit cell.

V_{pc} of the *Pc* and *R3c* phases are plotted in **Figure S4** against temperature; V_{pc} was calculated by dividing the lattice

volume by Z ($Z=4$ for *Pc* and $Z=6$ for *R3c*). A continuous change in V_{pc} across the *Pc*–*R3c* transition is indicative of a second-order phase transition, consistent with the group theoretical analysis.

The Rietveld plot of the *R3c* CuNbO₃ at 470 K is shown in **Figure 9a**. The refined structure is displayed in **Figure 9b** and the refined structural parameters are given in **Table 3**. The Nb1 position is fixed to (0, 0, 0). We refined the cation site occupancies to confirm deviations in the stoichiometry, and detected a small Cu defect ($g(\text{Cu})=0.929(9)$). This nonstoichiometric composition model (Cu_{0.93}NbO₃) leads to better overall fits than the stoichiometric composition model (CuNbO₃); $R_{wp} = 7.91\%$ and $R_B = 7.11\%$ for Cu_{0.93}NbO₃ and $R_{wp} = 7.92\%$ and $R_B = 11.4\%$ for CuNbO₃. The formation of Cu deficiency is related to the onset of the decomposition of the *R3c* phase as mentioned below, which is driven by the release of A-site Cu. The calculated spontaneous polarization along [001] ($= [111]_{pc}$) for *R3c* Cu_{0.93}NbO₃ is $15 \mu\text{C cm}^{-2}$, which is larger than that of the lower-symmetry *Pc* CuNbO₃. The counterintuitive result is due to the fact that the almost antiparallel off-center displacements of Nb⁵⁺ ions in *Pc* CuNbO₃ cancel each other's polarization. It should be mentioned that the *R3c* phase starts to decompose at around 500 K to produce Cu₂O and CuNb₂O₆, according to the temperature-variable SXRD experiments. The former compound, Cu₂O, is formed by the release of A-site Cu in the *R3c* phase and its subsequent oxidation by atmospheric oxygen. The latter compound, CuNb₂O₆, is isostructural to a perovskite-type CuTa₂O₆ (cubic or pseudo-cubic).^{60, 61} The thermal stability temperature range of *R3c* phase is so narrow that the *Pc*–*R3c* phase transition almost concurs with the decomposition reaction of the *R3c* phase. Given the nominal cation valences of the final decomposition product (Cu²⁺Nb⁵⁺₂O₆), we believe that a partial oxidation of Cu⁺ to Cu²⁺ (Cu^{+0.86}Cu²⁺_{0.07}Nb⁵⁺O₃) will occur in *R3c* Cu_{0.93}NbO₃ to compensate for its Cu vacancies.

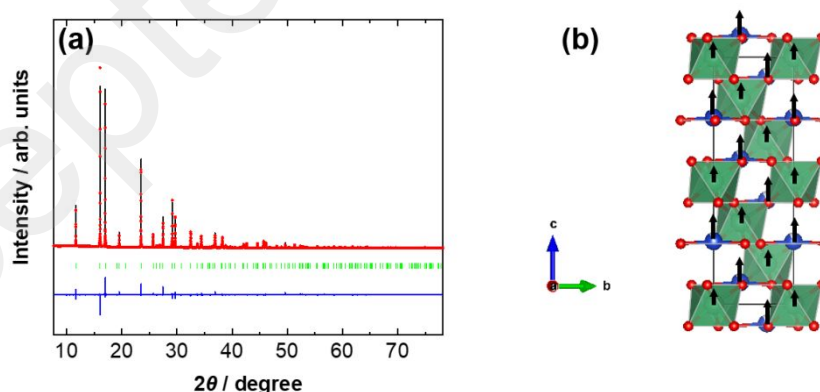


Figure 9. (a) Rietveld refinements against SXRD patterns ($\lambda = 0.77565 \text{ \AA}$) of HP-CuNbO₃ at 470 K. The refinement was performed on the basis of the rhombohedral *R3c* perovskite-type structure model with A-site deficiency (i.e., LiNbO₃-type Cu_{0.93}NbO₃), showing the observed (red circles) and calculated (black solid lines) profiles. The blue solid lines represent the difference between the observed and calculated profiles. The green ticks correspond to the positions of the allowed Bragg reflections. Peaks due to Cu₂O and CuNb₂O₆ were excluded in the refinement. (b) The refined crystal structure of *R3c* (LiNbO₃-type) Cu_{0.94}NbO₃ at 470 K. The arrows indicate the cation displacements from the closed-packed oxygen planes and those from the centroids of NbO₆ octahedra.

Table 3. Structural Parameters of HP-CuNbO₃ at 470 K Obtained from Refinements against the SXRD Data

atom	site	<i>g</i>	<i>x</i>	<i>y</i>	<i>z</i>	<i>U</i> _{eq/iso} / Å ²
Cu1	6 <i>a</i>	0.929(9)	0	0	0.255(3)	0.035(3)
Nb1	6 <i>a</i>	1	0	0	0	0.0166(7)
O1	18 <i>b</i>	1	0.078(3)	0.352(5)	0.078(2)	0.01665(1)

Space group: *R3c* (No. 161), *Z* = 6. Cu_{0.93}NbO₃ (fw = 199.9 g mol⁻¹): λ = 0.77565 Å, 0.615 Å < *d* < 6.03 Å; lattice parameters: *a* = 5.2433(2) Å, *c* = 14.0006(4) Å, and *V* = 333.34(2) Å³, *R*_{wp} = 7.91%, *R*_B = 7.11%. Cu1 and Nb1 were refined anisotropically.

4. DISCUSSION

As described above, we find two new polar polymorphs of CuNbO₃. One is the monoclinic *Pc* perovskite-type phase (HP-CuNbO₃) stabilized via the high-pressure and high-temperature synthesis, and the other the rhombohedral *R3c* perovskite-type (or LiNbO₃-type) phase obtained by heating the *Pc* phase in ambient pressure. The former is the first example of a simple *ABO*₃ perovskite crystallizing in monoclinic *Pc* symmetry with *a* ≈ √2*a*_{pc}, *b* ≈ √2*a*_{pc}, and *c* ≈ 2*a*_{pc} unit cell. It also represents a rare example of “noncollinear ferrielectric” dipole order. Here, it should be noted that, in contrast to the *Pc* phases, the higher-symmetry *R3c* phases have been often observed in *ABO*₃ compounds by the use of high-temperature and high-pressure conditions; examples include CuTaO₃,³² AFeO₃ (*A* = Sc,⁶² Ga,⁶³ and In⁶⁴), ATiO₃ (*A* = Mg,⁶⁵ Mn,^{66, 67} Fe,^{65, 68} Zn,⁶⁹ and Hg^{70, 71}), AGeO₃ (*A* = Mg,^{72, 73} Fe,⁷⁴ and Zn⁷³), ASnO₃ (*A* = Mn⁶⁸ and Zn⁷⁴), LiBO₃ (*B* = Sb,⁷⁶ W,⁷⁷ and Os⁵⁹), Pb- and Bi-containing perovskites^{78–83}, and cation mixed perovskites.^{83–88} To examine the stable structure of HP-CuNbO₃, we subsequently performed phonon calculations using the polar *R3c* phase as the parent structure. The crystal structure was optimized in the *R3c* symmetry. Phonon dispersion curves for the *R3c* structure are shown in **Figure 10**. We see an imaginary mode at the F point of the Brillouin zone. Within the framework of a second-order phase transition, freezing of the F-point softmode yields a monoclinic polar *Pc* structure with *a* ≈ √2*a*_{pc}, *b* ≈ √2*a*_{pc}, *c* ≈ 2*a*_{pc} and β ≈ 95°, leading to the antiparallel off-center displacements of Nb⁵⁺ and the *a*–*a*–*c*-type tilts of NbO₆ octahedra. Our calculations demonstrate that the *Pc* structure has a lower energy than the *R3c* structure and is dynamically stable, consistent with the experimental observation that the low-temperature and high-temperature phases of HP-CuNbO₃ crystallize in the space groups *Pc* and *R3c*, respectively.

It is worth emphasizing that HP-CuNbO₃ (*Pc*) has a lower-symmetry structure than LiNbO₃ (*R3c*), despite the very close *t* values between CuNbO₃ (*t* = 0.89) and LiNbO₃ (*t* = 0.85). Comparing the crystal structure of CuNbO₃ and LiNbO₃ (see **Figure 11**) reveals that *A*-site cations (Cu⁺ in

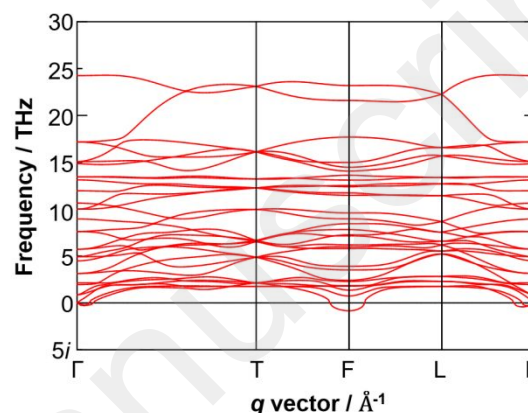


Figure 10. Phonon dispersion curves of HP-CuNbO₃ calculated with the *R3c* symmetry.

(a) Cu in *Pc* CuNbO₃



(b) Li in *R3c* LiNbO₃

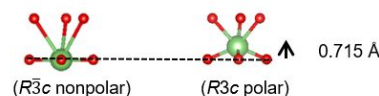


Figure 11. Short distance coordination around (a) Cu in HP-CuNbO₃ (this work) and (b) Li in LiNbO₃ (from Ref. 21). The light green, blue, and red spheres correspond to Li, Cu, and O atoms, respectively.

CuNbO₃ and Li⁺ in LiNbO₃) are displaced from the closed-packed oxygen planes along [111]_{pc}, but the Li displacements are much larger than the Cu displacements. While the Li displacements in *R3c* LiNbO₃ lead to the formation of LiO₆ octahedra (see **Figure 11b**), the relatively

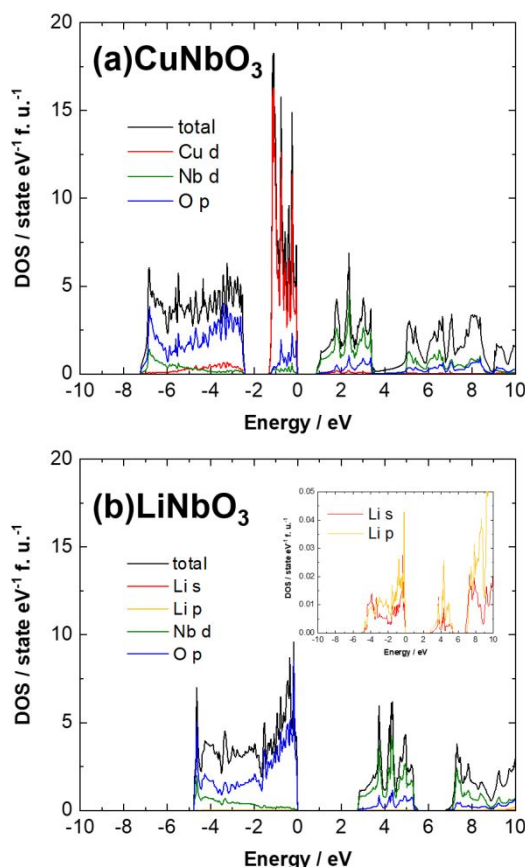


Figure 12. The calculated projected total and partial density of states (DOS) of *R3c* (a) CuNbO_3 and (b) LiNbO_3 . The zero of energy is set to the top of the valence band. The inset of (b) shows an enlarged view of the partial DOS of Li 4s and Li 4p states.

small Cu displacements in HP- CuNbO_3 confine the Cu–O bonds to three oxide ions forming triangles (see **Figure 11a**), i.e., Cu^+ ions are virtually three-coordinated in HP- CuNbO_3 . This may be explained by the difference in the bonding character between Li–O (ionic) and Cu–O (covalent).

To evaluate comparatively the bonding character for HP- CuNbO_3 and LiNbO_3 , we also calculated their electronic structures. In the calculations, we utilized the same *R3c* structure as that used in the phonon calculations. **Figure 12a, b** depicts the calculated total and partial density of states (DOS) for *R3c* CuNbO_3 and LiNbO_3 , respectively. For CuNbO_3 , the valence band mainly consists of Cu 3d and O 2p states, and the conduction band is composed of the Nb 4d state. The Cu 3d state contributes to the formation of the top of valence band through the orbital overlap with the O 2p state (see **Figure 12a**). This is in striking contrast to LiNbO_3 , where the valence band is composed of the O 2p state, without any significant participation of Li orbitals (see **Figure 12b**). Thus, the covalent bond character of A-site cations is obvious for CuNbO_3 . Note that the Nb 4d states of

CuNbO_3 and LiNbO_3 , which are completely empty in the ionic limits, are slightly occupied through orbital overlap with the O 2p states, forming the bottom of the valence band. This is indicative of the Nb–O covalency that drives the second-order Jahn–Teller effect. We believe that the covalent character of Cu–O and Nb–O bonds will be associated with the appearance of the noncollinear ferrielectric cation displacements as observed for HP- CuNbO_3 .

5. CONCLUSION

A novel perovskite-type oxide, CuNbO_3 , has been synthesized at 12 GPa and 1273 K. It forms a monoclinic *Pc* structure at 300 K, representing a rare example of a “noncollinear ferrielectric” dipole order. The *Pc* phase transforms to a “collinear ferroelectric” *R3c* structure upon heating at 470 K. The noncollinear ferrielectric (*Pc*)–collinear ferroelectric (*R3c*) transition is of displacive origin, and the condensing soft mode responsible for the phase transition is observed at the F point of the rhombohedral Brillouin zone, which corresponds to the structural distortion mainly due to the antiparallel off-center Nb displacements and the $a^-a^-c^-$ NbO_6 octahedral tilting. The original distortion within the monoclinic *Pc* perovskite phase, in particular with respect to LiNbO_3 , is explained on the basis of bonding character, as highlighted by electronic structure calculations.

ASSOCIATED CONTENT

Supporting Information

The Supporting Information is available free of charge on the ACS Publications website at DOI: XXXX.

Dependence of sample quality on synthesis pressures, oscilloscope traces of the SHG signals, and detailed structural analysis results (selected bond lengths and angles, and lattice parameters at various temperatures).

Accession Codes

CCDC 1977808 contains the supplementary crystallographic data for this paper. These data can be obtained free of charge via www.ccdc.cam.ac.uk/data_request/cif, or by emailing data_request@ccdc.cam.ac.uk, or by contacting The Cambridge Crystallographic Data Centre, 12 Union Road, Cambridge CB2 1EZ, UK; fax: +44 1223 336033.

AUTHOR INFORMATION

Corresponding Author

*Email for K.F.: fujita.koji.5w@kyoto-u.ac.jp

Present Address

[†](M.F.) Laboratory for Materials and Structures, Institute of Innovative Research, Tokyo Institute of Technology, Yokohama 226-8503, Japan

Author Contributions

All authors have given approval to the final version of the manuscript.

Funding Sources

This work was financially supported by JSPS KAKENHI Grant-in-Aids for Scientific Research (A) (Grant No. 17H01320) and (B) (Grant No. 19H02433), and Challenging Research (Exploratory) (Grant No. 18K18940). K. F. also thanks a grant from The Murata Science Foundation.

ACKNOWLEDGEMENT

SXRD experiments were performed on BL02B2 (Proposal Nos. 2019A1071 and 2019B1384) at SPring-8 with the approval of JASRI. XANES experiments were carried out on BL14B2 (Proposal Nos. 2017B1900 and 2019A1650). NPD experiments at D2B were supported by a beam time allocation from Institut Laue-Langevin (Proposal No. 5-23-714); doi:10.5291/ILL-DATA.5-23-714). The authors thank Suguru Yoshida and Jinsuke Miyake for their help with the NPD measurements.

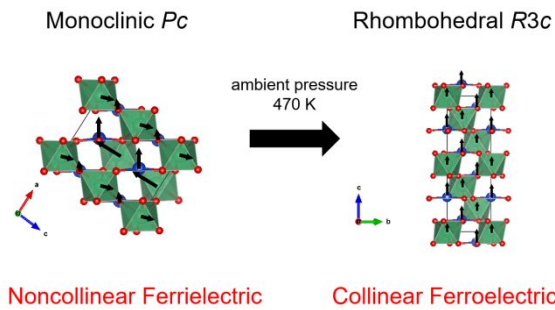
REFERENCES

- Saito, Y.; Takao, H.; Tani, T.; Nonoyama, T.; Takatori, K.; Homma, T.; Nagaya, T.; Nakamura, M. Lead-free piezoceramics. *Nature* **2004**, *432*, 84–87.
- Zuo, R.; Rödel, J.; Chen, R.; Li, L. Sintering and electrical properties of lead-free $\text{Na}_{0.5}\text{K}_{0.5}\text{NbO}_3$ piezoelectric ceramics. *J. Am. Ceram. Soc.* **2006**, *89*, 2010–2015.
- Wu, J.; Xiao, D.; Zhu, J. Potassium–Sodium Niobate Lead-Free Piezoelectric Materials: Past, Present, and Future of Phase Boundaries. *Chem. Rev.* **2015**, *115*, 2559–2595.
- Cohen, D.A.; Hossein-Zadeh, D.A.; Levi, A.F.J. High-Q microphotonic electro-optic modulator. *Solid State Electron.* **2001**, *45*, 1577–1589.
- Liu, J. W.; Chen, G.; Li, Z. H.; Zhang, Z.G. Hydrothermal synthesis and photocatalytic properties of ATaO_3 and ANbO_3 (A = Na and K). *Int. J. Hydrogen Energy* **2007**, *32*, 2269–2272.
- Shi, H.; Zou, Z. Photophysical and photocatalytic properties of ANbO_3 (A=Na, K) photocatalysts. *J. Phys. Chem. Solids* **2012**, *73*, 788–792.
- Huan, Y.; Shen, H.; Zhu, Y.; Li, M.; Li, H.; Wang, Z.; Hao, Y.; Wei, T. Enhanced ferro-photocatalytic performance for ANbO_3 (A = Na, K) nanoparticles. *Math. Biosci. Eng.* **2019**, *16*, 4122–4134.
- Brese, N. E.; O'keefe, M. Bond-Valence Parameters for Solids. *Acta Cryst.* **1991**, *B47*, 192–197.
- Shirane, G.; Danner, H.; Pavlovic, A.; Pepinsky, R. Phase Transitions in Ferroelectric KNbO_3 . *Phys. Rev.* **1954**, *93*, 672–673.
- Postnikov, A. V.; Neumann, T.; Borstel, G. Ferroelectric structure of KNbO_3 and KTaO_3 from first-principles calculations. *Phys. Rev. B* **1993**, *48*, 5910–5918.
- Kawamura, S.; Magome, E.; Moriyoshi, C.; Kuroiwa, Y.; Taniguchi, N.; Tanaka, H.; Maki, S.; Takata, M.; Wada, S. Electronic Polarization in KNbO_3 Visualized by Synchrotron Radiation Powder Diffraction. *Jpn. J. Appl. Phys.* **2013**, *52*, 09KF04.
- Cohen, R. E. Origin of ferroelectricity in perovskite oxides. *Nature* **1992**, *358*, 136–138.
- Kunz, M.; Brown, I. D. Out-of-Center Distortions around Octahedrally Coordinated d^0 Transition Metals. *J. Solid State Chem.* **1995**, *115*, 395–406.
- Ok, K. M.; Halasyamani, P. S.; Casanova, D.; Llunell, M.; Alemany, P.; Alvarez, S. Distortions in Octahedrally Coordinated d^0 Transition Metal Oxides: A Continuous Symmetry Measures Approach. *Chem. Mater.* **2006**, *18*, 3176–3183.
- Abrahams, S. C.; Reddy, J. M.; Bernstein, J. L. Ferroelectric Lithium Niobate. 3. Single Crystal X-Ray Diffraction study at 24°C. *J. Phys. Chem. Solids* **1966**, *27*, 997–1012.
- Weis, R. S.; Gaylord, T. K. Lithium Niobate: Summary of Physical Properties and Crystal Structure. *Appl. Phys. A.* **1985**, *37*, 191–203.
- A. M. Glazer, The Classification of Tilted Octahedra in Perovskites. *Acta Cryst.* **1972**, *B28*, 3384–3392.
- Sakowski-Cowley, A. C.; Łukaszewicz, K.; Megaw, H. D. The Structure of Sodium Niobate at Room Temperature, and the Problem of Reliability in Pseudosymmetric Structures. *Acta Cryst.* **1969**, *B25*, 851–865.
- Megaw, H. D. The seven phases of sodium niobate. *Ferroelectrics* **1974**, *7*, 87–89.
- Mishra, S. K.; Choudhury, N.; Chaplot, S. L.; Krishna, P. S. R.; Mittal, R. Competing antiferroelectric interaction in NaNbO_3 : Neutron diffraction and theoretical studies. *Phys. Rev. B* **2007**, *76*, 024110.
- Koruz, J.; Tellier, J.; Malič, B.; Bobnar, V.; Kosec, M. Phase transitions of sodium niobate powder and ceramics, prepared by solid state synthesis. *J. Appl. Phys.* **2010**, *108*, 113509.
- Johnston, K. E.; Tang, C. C.; Parker, J. E.; Knight, K. S.; Lightfoot, P.; Ashbrook, S. E. The Polar Phase of NaNbO_3 : A Combined Study by Powder Diffraction, Solid-State NMR, and First-Principles Calculations. *J. Am. Chem. Soc.* **2010**, *132*, 8732–8746.
- Fábry, J.; Zikmund, Z.; Kania, A.; Petříček, V. Silver niobium trioxide, AgNbO_3 . *Acta Cryst.* **2000**, *C56*, 916–918.
- Sciau, P.; Kania, A.; Dkhil, B.; Suard, E.; Ratuszna, A. Structural investigation of AgNbO_3 phases using x-ray and neutron diffraction. *J. Phys.: Condens. Matter* **2004**, *16*, 2795–2810.
- Fu, D.; Endo, M.; Taniguchi, H.; Taniyama, T.; Itoh, Mitsuru. AgNbO_3 : A lead-free material with large polarization and electromechanical response. *Appl. Phys. Lett.* **2007**, *90*, 252907.
- Yashihma, M.; Matsuyama, S.; Sano, R.; Itoh, M.; Tsuda, K.; Fu, D. Structure of Ferroelectric Silver Niobate AgNbO_3 . *Chem. Mater.* **2011**, *23*, 1643–1645.
- Yashima, M.; Matsuyama, S. Origin of the Ferroelectricity and Visible-Light Photocatalytic Activity of Silver Niobate AgNbO_3 . *J. Phys. Chem. C* **2012**, *116*, 24902–24906.
- Joshi, U. A.; Palasyuk, A. M.; Maggard, P. A. Photoelectrochemical Investigation and Electronic Structure of a p-Type CuNbO_3 Photocathode. *J. Phys. Chem. C* **2011**, *115*, 13534–13539.
- Harb, M.; Masih, D.; Takanabe, K. Screened coulomb hybrid DFT investigation of band gap and optical absorption predictions of CuVO_3 , CuNbO_3 and $\text{Cu}_5\text{Ta}_{11}\text{O}_{30}$ materials. *Phys. Chem. Chem. Phys.* **2014**, *16*, 18198–18204.
- Pralong, V.; Reddy, M. A.; Caignaert, V.; Malo, S.; Lebedev, O. I.; Varadaraju, U. V.; Raveau, B. A New Form of LiNbO_3 with a Lamellar Structure Showing Reversible Lithium Intercalation. *Chem. Mater.* **2011**, *23*, 1915–1922.
- Rodgers, J. A.; Williams, A. J.; Attfield, J. P. High-pressure / High-temperature Synthesis of Transition Metal Oxide Perovskites. *Z. Naturforsch. B*, **2014**, *61*, 1515–1526.
- Belik, A. A.; and Yi, W. High-pressure synthesis, crystal chemistry and physics of perovskites with small cations at the A site. *J. Phys.: Condens. Matter* **2014**, *26*, 163201.
- Sleight, A. W.; Prewitt, C. T. Preparation of CuNbO_3 and CuTaO_3 at high pressure. *Mater. Res. Bull.* **1970**, *5*, 207–212.
- Rodríguez-Carvajal, J. Recent advances in magnetic structure determination by neutron powder diffraction. *Physica* **1993**, *B192*, 55–69.

- 35) Petříček, V.; Dušek, M.; Palatinus, L. Crystallographic Computing System JANA2006: General features. *Z. Kristallogr.* **2014**, *229*, 345–352.
- 36) Louër, D.; Boulton, A. Powder pattern indexing and the dichotomy algorithm. *Z. Kristallogr. Suppl.* **2007**, *26*, 191–196.
- 37) Altomare, A.; Cuocci, C.; Giacovazzo, C.; Moliterni, A.; Rizzi, R.; Corriero, N.; Falcicchio, A. *EXPO2013*: a kit of tools for phasing crystal structures from powder data. *J. Appl. Cryst.* **2013**, *46*, 1231–1235.
- 38) Izumi, F.; Momma, K. *VESTA 3* for three-dimensional visualization of crystal, volumetric and morphology data. *J. Appl. Cryst.* **2011**, *44*, 1272–1276.
- 39) Blöchl, P. E. Projector augmented-wave method. *Phys. Rev. B* **1994**, *50*, 17953–17979.
- 40) Kresse, G.; Hafner, J. *Ab initio* molecular dynamics for open-shell transition metals. *Phys. Rev. B* **1993**, *48*, 13115–13118.
- 41) Kresse, G.; Furthmüller, J. Efficient iterative schemes for *ab initio* total-energy calculations using a plane-wave basis set. *Phys. Rev. B* **1996**, *54*, 11169–11186.
- 42) Kresse, G.; Joubert, D. From ultrasoft pseudopotentials to the projector augmented wave method. *Phys. Rev. B* **1999**, *59*, 1758–1775.
- 43) Monkhorst, H. J.; Pack, J. D. Special points for Brillouin-zone integrations. *Phys. Rev. B* **1976**, *13*, 5188–5192.
- 44) Perdew, J. P.; Ruzsinszky, A.; Csonka, G. I.; Vydrov, O. A.; Scuseria, G. E.; Constantin, L. A.; Zhou, X.; Burke, K. Restoring the Density-Gradient Expansion for Exchange in Solids and Surfaces. *Phys. Rev. Lett.* **2008**, *100*, 136406.
- 45) Dudarev, S. L.; Botton, G. A.; Savrasov, S. Y.; Humphreys, C. J.; Sutton, A. P. Electron-energy-loss spectra and the structural stability of nickel oxide: An LSDA+U study. *Phys. Rev. B* **1998**, *57*, 1505–1509.
- 46) Togo, A.; Oba, F.; Tanaka, I. Transition pathway of CO₂ crystals under high pressures. *Phys. Rev. B* **2008**, *77*, 184101.
- 47) Togo, A.; Oba, F.; Tanaka, I. First-principles calculations of the ferroelastic transition between rutile-type and CaCl₂-type SiO₂ at high pressures. *Phys. Rev. B* **2008**, *78*, 134106.
- 48) Togo, A.; Tanaka, I. Evolution of crystal structures in metallic elements. *Phys. Rev. B*, **2013**, *87*, 184104.
- 49) Akamatsu, H.; Fujita, K.; Kuge, T.; Gupta, A. S.; Togo, A.; Lei, S.; Xue, F.; Stone, G.; Rondinelli, J. M.; Chen, L. Q.; Tanaka, I.; Gopalan, V.; Tanaka, K. Inversion Symmetry Breaking by Oxygen Octahedral Rotations in the Ruddlesden-Popper NaRTiO₄ Family. *Phys. Rev. Lett.* **2014**, *112*, 187602.
- 50) Togo, A.; Tanaka, I. First principles phonon calculations in materials science. *Scr. Mater.* **2015**, *108*, 1–5.
- 51) Anisimov, V. I.; Solovyev, I. V.; Korotin, M. A.; Czyżyk, M. T.; Sawatzky, G. A. Density-functional theory and NiO photoemission spectra. *Phys. Rev. B* **1993**, *48*, 16929–16934.
- 52) Schwarz, K.; Blaha, P.; Madsen, G. K. H. Electronic structure calculations of solids using the WIEN2k package for material sciences. *Comput. Phys. Commun.* **2002**, *147*, 71–76.
- 53) Krause, M. O.; Oliver, J. H. Natural widths of atomic *K* and *L* levels, *K* α X-ray lines and several *KLL* Auger lines. *J. Phys. Chem. Ref. Data* **1979**, *8*, 329–338.
- 54) Campbell, B. J.; Stokes, H. T.; Tanner, D. E.; Hatch, D. M. ISODISPLACE: a web-based tool for exploring structural distortions. *J. Appl. Cryst.* **2006**, *39*, 607–614.
- 55) Abrahams, S. C.; Marsh, P. Defect Structure Dependence on Composition in Lithium Niobate. *Acta Cryst.* **1986**, *B42*, 61–68.
- 56) Iyi, N.; Kitamura, K.; Izumi, F.; Yamamoto, J. K.; Hayashi, T.; Asano, H.; Kimura, S. Comparative study of defect structures in lithium niobate with different compositions. *J. Solid State Chem.* **1992**, *101*, 340–352.
- 57) Salje, E. K. H.; Rehmann, S.; Pobell, F.; Morris, D.; Knight, K. S.; Herrmannsdörfer, T.; Dove, M. T. Crystal structure and paramagnetic behaviour of ϵ -WO_{3-x}. *J. Phys.: Condens. Matter* **1997**, *9*, 6563–6577.
- 58) Sugii, K.; Koizumi, H.; Miyazawa, S.; Kondo, S. Temperature variations of lattice parameters of LiNbO₃, LiTaO₃ and Li(Nb_{1-y}Ta_y)O₃ solid-solutions. *J. Cryst. Growth* **1976**, *33*, 199–202.
- 59) Shi, Y.; Guo, Y.; Wang, X.; Princep, A. J.; Khalyavin, D.; Manuel, P.; Michiue, Y.; Sato, A.; Tsuda, K.; Yu, S.; Arai, M.; Shirako, Y.; Akaogi, M.; Wang, N.; Yamaura, K.; Boothroyd, A. T. A ferroelectric-like structural transition in a metal. *Nat. Mater.* **2013**, *12*, 1024–1027.
- 60) Propach, V. Kristallstruktur von Ca_{0.5}Cu_{1.5}Ti₂O₆, Cu_{1.5}TaTiO₆ und CuTa₂O₆. Das spektroskopische Verhalten von Cu²⁺-Ionen in kuboktaedrischer Umgebung. *Z. anorg. allg. Chem.* **1977**, *435*, 161–171.
- 61) Ebbinghaus, S. G. Influence of composition and thermal treatment on the properties of Cu_{2+x}Ta₄O_{12+x}. *Prog. Solid State Chem.* **2007**, *35*, 421–431.
- 62) Kawamoto, T.; Fujita, K.; Yamada, I.; Matoba, T.; Kim, S. J.; Gao, P.; Pan, X.; Findlay, S. D.; Tassel, C.; Kageyama, H.; Studer, A. J.; Hester, J.; Irfune, T.; Akamatsu, H.; Tanaka, K. Room-temperature polar ferromagnet ScFeO₃ transformed from a high-pressure orthorhombic perovskite phase. *J. Am. Chem. Soc.* **2014**, *136*, 15291–15299.
- 63) Niu, H.; Pitcher, A. J.; Corkett, A. J.; Ling, S.; Mandal, P.; Zanella, M.; Dawson, K.; Stamenov, P.; Batuk, D.; Abakumov, A. M.; Bull, C. L.; Smith, R. I.; Murray, C. A.; Day, S. J.; Slater, B.; Cora, F.; Claridge, J. B.; Rosseinsky, M. J. Room Temperature Magnetically Ordered Polar Corundum GaFeO₃ Displaying Magnetoelectric Coupling. *J. Am. Chem. Soc.* **2017**, *139*, 1520–1531.
- 64) Fujita, K.; Kawamoto, T.; Yamada, I.; Hernandez, O.; Hayashi, N.; Akamatsu, H.; Lafargue-Dit-Hauret, W.; Rocquefelte, X.; Fukuzumi, M.; Manuel, P.; Studer, A. J.; Knee, C. S.; Tanaka, K. LiNbO₃-type InFeO₃: Room-temperature polar magnet without second-order Jahn-Teller active ions. *Chem. Mater.* **2016**, *28*, 6644–6655.
- 65) Linton, J. A.; Fei, Y.; Navrotsky, A. Complete Fe-Mg solid solution in lithium niobate and perovskite structures in titanates at high pressures and temperatures. *Am. Mineral.* **1997**, *82*, 639–642.
- 66) Ko, J.; and Prewitt, C. T. High-pressure phase transition in MnTiO₃ from the ilmenite to the LiNbO₃ structure. *Phys. Chem. Miner.* **1988**, *15*, 355–362.
- 67) Aimi, A.; Katsumata, T.; Mori, D.; Fu, D.; Itoh, M.; Kyomen, T.; Hiraki, K.; Takahashi, T.; Inaguma, Y. High-Pressure Synthesis and Correlation between Structure, Magnetic, and Dielectric Properties in LiNbO₃-Type MnMO₃ (M = Ti, Sn). *Inorg. Chem.* **2011**, *50*, 6392–6398.
- 68) Leinenweber, K.; Utsumi, W.; Tsuchida, Y.; Yagi, T.; Kurita, K. Unquenchable High-Pressure Perovskite Polymorphs of MnSnO₃ and FeTiO₃. *Phys. Chem. Miner.* **1991**, *18*, 244–250.
- 69) Inaguma, Y.; Aimi, A.; Shirako, Y.; Sakurai, D.; Mori, D.; Kojitani, H.; Akaogi, M.; Nakayama, M. High-pressure synthesis, crystal structure, and phase stability relations of a LiNbO₃-type polar titanate ZnTiO₃ and its reinforced polarity by the second-order Jahn-Teller effect. *J. Am. Chem. Soc.* **2014**, *136*, 2748–2756.
- 70) Sleight, A. W.; Prewitt, C. T. High-Pressure HgTiO₃ and HgPbO₃: Preparation, Characterization, and Structure. *J. Solid State Chem.* **1973**, *6*, 509–512.
- 71) Shan, Y. J.; Inaguma, Y.; Tetsuka, H.; Nakamura, T.; Gauckler, L. J. Synthesis and Phase Transition of HgTiO₃. *Ferroelectrics* **2006**, *337*, 71–76.
- 72) Leinenweber, K.; Wang, Y.; Yagi, T.; Yusa, H. An unquenchable perovskite phase of MgGeO₃ and comparison with MgSiO₃ perovskite. *Am. Mineral.* **1994**, *79*, 197–199.

- 73) Akaogi, M.; Kojitani, H.; Yusa, H.; Yamamoto, R.; Kido, M.; Koyama, K. High-pressure transitions and thermochemistry of MGeO_3 (M=Mg, Zn and Sr) and Sr-silicates: systematics in enthalpies of formation of $\text{A}^{2+}\text{B}^{4+}\text{O}_3$ perovskites. *Phys. Chem. Miner.* **2005**, *32*, 603–613.
- 74) Hattori, T.; Matsuda, T.; Tsuchiya, T.; Nagai, T.; Yamanaka, T. Clinopyroxene-perovskite phase transition of FeGeO_3 under high pressure and room temperature. *Phys. Chem. Miner.* **1999**, *26*, 212–216.
- 75) Inaguma, Y.; Yoshida, M.; Katsumata, T. A polar oxide ZnSnO_3 with a LiNbO_3 -type structure. *J. Am. Chem. Soc.* **2008**, *130*, 6704–6705.
- 76) Inaguma, Y.; Aimi, A.; Mori, D.; Katsumata, T.; Ohtake, M.; Nakayama, M.; Yonemura, M. High-Pressure Synthesis, Crystal Structure, Chemical Bonding, and Ferroelectricity of LiNbO_3 -Type LiSbO_3 . *Inorg. Chem.* **2018**, *57*, 15462–15473.
- 77) Ishida, K.; Ikeuchi, Y.; Tassel, C.; Takatsu, H.; Brown, C. M.; Kageyama, H. High-Pressure Synthesis of Non-Stoichiometric Li_xWO_3 ($0.5 \leq x \leq 1.0$) with LiNbO_3 Structure. *Inorganics* **2019**, *7*, 63.
- 78) Belik, A. A.; Wuernisha, T.; Kamiyama, T.; Mori, K.; Maie, M.; Nagai, T.; Matsui, Y.; Takayama-Muromachi, E. High-Pressure Synthesis, Crystal Structures, and Properties of Perovskite-like BiAlO_3 and Pyroxene-like BiGaO_3 . *Chem. Mater.* **2006**, *18*, 133–139.
- 79) Inaguma, Y.; Yoshida, M.; Tsuchiya, T.; Aimi, A.; Tanaka, K.; Katsumata, T.; Mori, D. High-pressure synthesis of novel lithium niobate type oxides. *J. Phys.: Conf. Ser.* **2010**, *215*, 012131.
- 80) Inaguma, Y.; Tanaka, K.; Tsuchiya, T.; Mori, D.; Katsumata, T.; Ohba, T.; Hiraki, K.; Takahashi, T.; Saitoh, H. Synthesis, Structural Transformation, Thermal Stability, Valence State, and Magnetic and Electronic Properties of PbNiO_3 with Perovskite and LiNbO_3 -Type Structures. *J. Am. Chem. Soc.* **2011**, *133*, 16920–16929.
- 81) Yu, R.; Hojo, H.; Mizoguchi, T.; Azuma, M. A new LiNbO_3 -type polar oxide with closed-shell cations: ZnPbO_3 . *J. Appl. Phys.* **2015**, *118*, 094103.
- 82) Mori, D.; Tanaka, K.; Saitoh, H.; Kikegawa, T.; Inaguma, Y. Synthesis, Direct Formation under High Pressure, Structure, and Electronic Properties of LiNbO_3 -type Oxide PbZnO_3 . *Inorg. Chem.* **2015**, *54*, 11405–11410.
- 83) Sakai, Y.; Nishikubo, T.; Ogata, T.; Ishizaki, H.; Imai, T.; Mizumaki, M.; Mizokawa, T.; Machida, A.; Watanuki, T.; Yokoyama, K.; Okimoto, Y.; Koshihara, S.; Das, H.; Azuma, M. Polar–Nonpolar Phase Transition Accompanied by Negative Thermal Expansion in Perovskite-Type $\text{Bi}_{1-x}\text{Pb}_x\text{NiO}_3$. *Chem. Mater.* **2019**, *31*, 4748–4758.
- 84) Belik, A. A.; Furubayashi, T.; Yusa, H.; Takayama-Muromachi, E. Perovskite, LiNbO_3 , Corundum, and Hexagonal Polymorphs of $(\text{In}_{1-x}\text{M}_x)\text{MO}_3$. *J. Am. Chem. Soc.* **2011**, *133*, 9405–9412.
- 85) Belik, A. A.; Yi, W.; Kumagai, Y.; Katsuya, Y.; Tanaka, M.; Oba, F. LiNbO_3 -Type Oxide $(\text{Tl}_{1-x}\text{Sc}_x)\text{ScO}_3$: High-Pressure Synthesis, Crystal Structure, and Electronic Properties. *Inorg. Chem.* **2016**, *55*, 1940–1945.
- 86) Li, M. R.; Walker, D.; Retuerto, M.; Sarkar, T.; Hadermann, J.; Stephens, P. W.; Croft, M.; Ignatov, A.; Grams, C. P.; Hemberger, J.; Nowik, I.; Halasyamani, P. S.; Tran, T. T.; Mukherjee, S.; Dasgupta, T. S.; Greenblatt, M. Polar and magnetic Mn_2FeMO_6 (M=Nb, Ta) with LiNbO_3 -type structure: High-pressure synthesis. *Angew. Chem. Int. Ed.* **2013**, *52*, 8406–8410.
- 87) Li, M. R.; Stephens, P. W.; Retuerto, M.; Sarkar, T.; Grams, C. P.; Hemberger, J.; Croft, M. C.; Walker, D.; Greenblatt, M. Designing Polar and Magnetic Oxides: $\text{Zn}_2\text{FeTaO}_6$ - in Search of Multiferroics. *J. Am. Chem. Soc.* **2014**, *136*, 8508–8511.
- 88) Han, Y.; Zeng, Y.; Hendrickx, M.; Hadermann, J.; Stephens, P. W.; Zhu, C.; Grams, C. P.; Hemberger, J.; Frank, C.; Li, S.; Wu, M.; Retuerto, M.; Croft, M.; Walker, D.; Yao, D. X.; Greenblatt, M.; Li, M. R. Universal A-Cation Splitting in LiNbO_3 -Type Structure Driven by Intrapositional Multivalent Coupling. *J. Am. Chem. Soc.* **2020**, *142*, 7168–7178.

For Table of Contents Only



Synopsis: Perovskite-type CuNbO_3 was synthesized at 12 GPa and 1473 K. It crystallizes in a polar monoclinic Pc space group. This Pc phase exhibits unusual noncollinear ferrielectric structure, due to parallel Cu displacements and antiparallel Nb displacements along different axes, representing a new type of polar phase in the perovskite structure. At about 470 K, it transforms into the collinear ferroelectric $R3c$ structure that features parallel Cu and Nb displacements in the same direction.